15th International Conference on Fluid Control, Measurements and Visualization
27-30 May, 2019, Naples, Italy

Application of Hot-film Anemometry to resolve the Unsteady Boundary Layer Transition of a Laminar Airfoil experiencing Limit Cycle Oscillations

Marc Braune[1,*] and **Stefan Koch**[2]

[1]DLR German Aerospace Center, Institute of Aeroelasticity, Bunsenstr. 10, 37073 Göttingen, Germany
[2]DLR German Aerospace Center, Institute of Aerodynamics and Flow Technology, Bunsenstr. 10, 37073 Göttingen, Germany
[*]corresponding author: Marc.Braune@dlr.de

Abstract The unsteady boundary layer behavior of a supercritical laminar airfoil model, which undergoes single degree of freedom limit cycle oscillations in pitch, is investigated by the application of hot-film anemometry. The data basis is a 2D flutter experiment under transonic flow conditions. The laminar airfoil model was elastically mounted with one degree of freedom in pitch and performed self-excited limit cycle oscillations at a Mach number of $Ma = 0.73$ and a Reynolds number of $Re \approx 2 \cdot 10^6$. An analysis of the hot-films on the basis of the quasi-wall shear stress is carried out, with which the boundary layer state for steady and unsteady flow is resolved. An algorithm is presented which allows an automated detection of the transition position, so that a relationship between airfoil model and transition motion can be quantified.
A sudden movement of the boundary layer transition is observed at the upper and lower reversal points of the limit cycle oscillation, while in parts of the up- and downstroke of the laminar airfoil a shock-induced transition occurs in combination with a laminar separation bubble. During the limit cycle oscillation, a delayed response of the boundary layer occurs, resulting in a significant phase lag between the motion of the boundary layer transition and the motion of the laminar airfoil.
Keywords: hot-film anemometry, laminar airfoil, boundary layer transition, limit cycle oscillation

1 Introduction

Laminar flow technologies are an ongoing object of research, as there is high potential of laminar airfoils to sufficiently reduce the fuel consumption and thus the emissions of modern aircraft. Driven by the related flow physics behind these techniques, new challenges arise for the field of aeroelasticity as discussed by Tichy et al. [1]. Since a transitional boundary layer flow is an inherent feature of laminar airfoils, the influence of various boundary layer effects like laminar-turbulent boundary layer transition and separation have to be considered when assessing the aeroelastic stability of these airfoils. Experimental investigations by Hebler [2] as well as numerical investigations by van Rooij and Wegner [3], Fehrs [4] and Fehrs et al. [5] showed that aeroelastic instabilities on a laminar airfoil occur earlier for a boundary layer with free transition than in a fully turbulent flow. In a 2D flutter experiment on a CAST 10 supercritical laminar airfoil model in the transonic flow regime, Braune and Hebler [6] further showed that self-excited single degree of freedom (1-DOF) limit cycle oscillations (LCOs) in pitch occurred in the vicinity of the characteristic laminar bucket of the airfoil. This aeroelastic instability is directly connected to a boundary layer that can perform a free laminar-turbulent boundary layer transition. In order to resolve the unsteady behavior of the boundary layer during LCOs, the suction side of the wind tunnel model was equipped with 26 hot-film sensors that were operated by constant temperature anemometers (CTA).

Surface mounted hot-film sensors are an established measurement technique for measuring wall shear stresses since the first investigations by Liepmann and Skinner [7] and Bellhouse and Schultz [8]. The application of multiple hot-film sensor (MHFS) arrays for the large-scale investigation of the boundary layer of bodies in flows is also well established and is particularly suitable for the more precise characterization of instability mechanisms in boundary layers due to the high dynamic response of the measurement technique, as it was done by Leuckert et al. [9], for example.

Lee and Basu [10] used MHFS to study the unsteady development of the boundary layer on an oscillating airfoil model at low Reynolds numbers. Further investigations of the unsteady boundary layer transition on pitching airfoils at higher Reynolds numbers but still subsonic Mach numbers were performed by Richter et al. [11] [12]. The transition position was detected by means of the root-mean-square (RMS) of the unfiltered

voltage signals of each hot-film sensor. The same statistical methods as well as a calculation of the skewness of the hot-film signals were applied by Mai and Hebler [13] and Hebler et al. [14] to investigate the unsteady behavior of the boundary layer on the CAST 10 laminar airfoil under transonic flow conditions. In all cases, a manual evaluation of the hot-film signals was carried out, which is very time-consuming. Based on the skweness, Richter et al. [15] [16] used an automated algorithm for the detection of unsteady laminar-turbulent boundary layer transition. The algorithm is described in more detail in Goerttler et al. [17]. This evaluation method was so far applied to cases with a low Mach number and without occurring compression shocks.

In this paper, the unsteady behavior of the boundary layer for a CAST 10 supercritical laminar airfoil is investigated, while the airfoil performs a 1-DOF LCO in pitch. The present boundary conditions, i.e. a transonic flow with a shock-boundary layer interaction as well as comparatively small oscillation amplitudes of less than $|\Delta\alpha| < 1^\circ$ and a high oscillation frequency of $f_\alpha \approx 60$ Hz of the LCO, thus deviate significantly from the cases investigated above. Therefore, a statistical interpretation of the hot-film signals can only be roughly done, especially when the shock position is located close to a hot-film sensor. In addition, the physical view is lost, as not only the boundary layer influences the hot-film signals anymore. Shock and boundary layer separation also lead to a change of the signals and manual data interpretation therefore requires a lot of experience.

However, in order to provide a physically motivated identification of the boundary layer states and in particular an automated detection of the laminar-turbulent boundary layer transition, an evaluation of the hot-films on the basis of the quasi-wall shear stress introduced by Hodson [18] is presented here. On this basis, an algorithm has been developed which allows a mostly automated detection of the laminar-turbulent boundary layer transition even under the mentioned flow conditions. For steady and unsteady flows, as with a LCO, the boundary layer and the shock-boundary layer interaction of the laminar airfoil are resolved for a Mach number of $\mathrm{Ma} = 0.73$ and a Reynolds number of $\mathrm{Re} \approx 2 \cdot 10^6$. In addition, a relation between the motion of the model and that of the boundary layer transition for transonic flow conditions is quantified for the first time.

2 Experimental test setup

The presented results were obtained by a 2D flutter experiment on a CAST 10 supercritical laminar airfoil model, carried out in the Transonic Wind Tunnel Goettingen (DNW-TWG). The measurements were performed in a Mach number range of $0.5 \leq \mathrm{Ma} \leq 0.8$ and a chord based Reynolds number of $1.15 \cdot 10^6 \leq \mathrm{Re} \leq 2.83 \cdot 10^6$. The mean angle of attack was preset to $\alpha \approx 0^\circ$, so that flutter measurements were performed directly within the charateristic laminar bucket of the airfoil. A detailed description of the experimental setup can be found in Braune and Hebler [6], so that only a brief overview of the flutter test setup is given below.

2.1 Flutter experiment

A CAST 10 laminar airfoil model with a chord length of $c = 0.3$ m and a span of $s = 0.997$ m was elastically mounted into a flutter test rig, which was previously used by Dietz et al. [19]. Two plate and torsion spring systems, one on each side of the wind tunnel wall, provided a two degree of freedom motion in heave and pitch. In order to study pure 1-DOF flutter, the heave springs were mechanically locked, so that the model solely performed motions in pitch around c/4. A sketch of the dynamical system is depicted in Fig. 1.

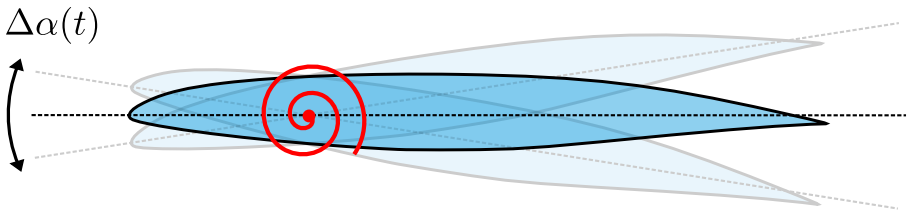

Fig. 1 Aeroelastic setup for 1-DOF flutter in pitch.

Several safety systems like brakes and a flutter controller allow investigations of aeroelastic systems at the

stability limit and even beyond. So, also LCOs or flutter with high grows rates in amplitude can be directly observed and recorded.

The pitch motion $\Delta\alpha(t)$ of the wind tunnel model was measured by laser triangulators with an accuracy of less than 0.02°. Aerodynamic forces and moments were calculated by a chordwise integration of the pressure distribution, obtained by 60 unsteady pressure sensors mounted into the model. All data were recorded with a sampling frequency of 2.4 kHz.

2.2 Hot-film anemometry

In order to resolve the unsteady behavior of the boundary layer, the suction side of the wind tunnel model is equipped with a multiple hot-film sensor (MHFS) array, consisting of 26 hot-film sensors that were operated by multiple constant temperature anemometers (CTAs). Each sensor is integrated into a Wheatstone bridge circuit, where it is set to an operating resistance R_S and thus heated to an operating temperature T_S. The bridge is aligned. Due to changing flow conditions, hence a changed heat transfer, the resistance of the hot-film sensor changes and an imbalance of the bridge is generated. The bridge restores the alignment by changing the bridge voltage U. If the gain of the anemometer is sufficiently high, the equilibrium of the bridge is restored immediately and the sensor resistance or temperature is kept constant. Each sensor consists of a 0.2 μm thin nickel film with 1.45 mm length and 0.1 mm width. The sensors are deposited onto a polyimide foil with a thickness of 50 μm and are connected to the CTA-system by copper coated leads. The MHFS substrate foil is embedded flush into the model surface to avoid steps and thus a forced transition induced by the MHFS array. So, the hot-films can be seen as a non-intrusive measurement technique.

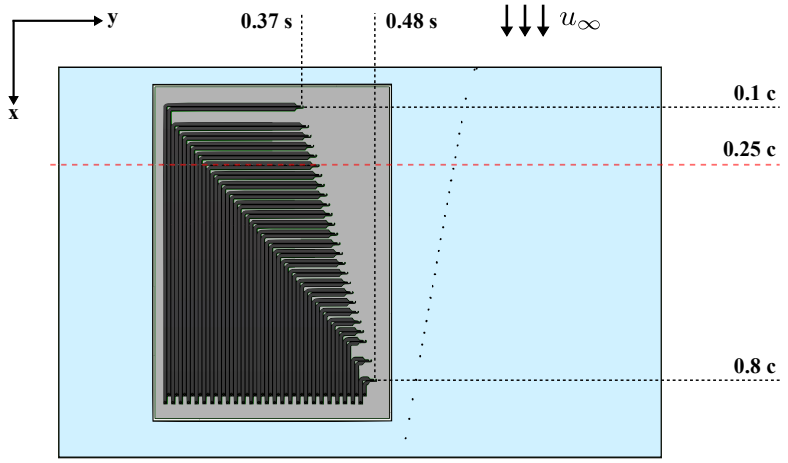

Fig. 2 MHFS array on the suction side of the CAST 10 airfoil model.

Figure 2 shows the location of the MHFS array close to the midsection on the suction side of the laminar airfoil model. The sensors cover a chord length of 0.1 c to 0.8 c. Their layout is staggered to avoid mutual interference by the temperature boundary layers caused by the convective heat dissipation of each sensor.

The hot-film sensors have a nominal resistance R_0 of approximately 9.1 Ω at ambient temperature. The overheat ratio $a = \frac{R_S}{R_0}$ was set to 1.3, so the heated hot-films reached a temperature difference to the ambient temperature T_a of $\Delta T = T_S - T_a \approx 100$ K.

The voltage signals of the CTAs were recorded with a separate data acquisition system with a sampling frequency of 120 kHz. In order to utilize the full sampling frequency, a rectangular test was carried out before each measuring day. Thereby, the stability of the CTA circuits were proved and the sensors were adjusted to high cut-off frequencies of approximately 60 kHz. Both data acquisition systems, one for the anemometry system and the second for the other sensors, were synchronized in time.

During a test run, the respective voltage signals of the CTAs were recorded, which corresponded to the heat flux, respectively the wall shear stress, at the hot-film sensors under the incoming flow. At the same time, the ambient temperature was measured, which is subject to fluctuations of up to 10 K during a measurement series

despite cooling of the wind tunnel. In addition, the zero voltages U_0 of the hot-film sensors in the heated state without inflow were recorded before and after each measurement series, i.e. before a change of the stagnation pressure in the wind tunnel. The latter voltage signals are necessary for further data processing, which is described in more detail in the following section.

3 Theoretical Overview and data processing

This section presents the theoretical background of the hot-film anemometry technique to establish a connection between the sensor signals and the state of the boundary layer. Since for practical reasons a calibration of a hot-film array is not possible within the experimental context presented here, quantitative wall shear stress measurements cannot be performed. For this purpose, the quasi-wall shear stress is introduced, which allows at least a qualitative and physically motivated interpretation, i.e. an indication of where the boundary layer transition and a separation of the boundary layer takes place.

3.1 Relation of heat transfer and wall shear stress

The theoretical foundation of the hot-film anemometry technique is based on the Reynolds analogy, i.e. the resemblance of impulse and heat transfer in viscous flows. Thus, a relation can be derived between the local wall shear stress τ_w and the heat transfer $\dot{Q}_F$ from a hot-film element to the flow. By theoretical analyses, considering dimensional and similarity conditions, Liepmann and Skinner [7] have shown that $\dot{Q}_F$ for a heated element with an effective length L can be written as

$$\dot{Q}_F \sim \left(\frac{c_p\,\lambda^2}{\nu}\right)^{\frac{1}{3}} \Delta T \int_0^L \left(\frac{\tau_w(x)}{x}\right)^{\frac{1}{3}} \mathrm{d}x\,, \tag{1}$$

where c_p denotes the specific isobar heat capacity, λ the thermal conductivity, ν the kinematic viscosity and ΔT the temperature difference between flow and heated hot-film element. For a small extension of the element in streamwise direction x, it is assumed that $\tau_w(x) \approx$ const., so the integral given in Eq. (1) can be reduced and thus

$$\int_0^L \left(\frac{\tau_w(x)}{x}\right)^{\frac{1}{3}} \mathrm{d}x \sim {\tau_w}^{\frac{1}{3}}\, L^{\frac{2}{3}} \quad \Rightarrow \quad \frac{\dot{Q}_F}{\Delta T} \sim {\tau_w}^{\frac{1}{3}}\,. \tag{2}$$

The energy balancing equation of a single hot-film sensor

$$\sum \dot{Q} = mc_s \frac{\mathrm{d}T_S}{\mathrm{d}t} + \dot{Q}_F + \dot{Q}_S - \frac{U(t)^2}{R_S} = 0 \tag{3}$$

is composed of the stored heat quantity per time $m\,c_s \frac{\mathrm{d}T}{\mathrm{d}t}$, the heat loss to the flow $\dot{Q}_F$ and to the carrier substrate $\dot{Q}_S$ as well as the supplied electrical power $P(t) = \frac{U(t)^2}{R_S}$. As the sensor is operated by a CTA, its resistance R_s and thus its temperature is kept constant, hence $\frac{\mathrm{d}T_S}{\mathrm{d}t} = 0$. By combining Eq. (1), (2) and (3) the wall shear stress can be written as

$$\tau_w \sim \left(\frac{\nu}{c_p\,\lambda^2\,L^2 {R_s}^3}\right)\left(\frac{U(t)^2 - R_S\dot{Q}_S}{\Delta T}\right)^3\,. \tag{4}$$

The occurring terms can be replaced by A and B in accordance with Bellhouse and Schultz [8], so that the wall shear stress yields

$$\tau_w = A\left(\frac{U(t)^2 - B^2}{\Delta T}\right)^3\,. \tag{5}$$

In general, A and B are functions of the temperature difference ΔT. Considering only small variations of ΔT, A and B can be assumed as constants, where the similarity of Eq. (5) to King's law [20], which is often used in hot-wire anemometry, should be noted here. For a quantitative measurement of the wall shear stress by hot-film anemometry, the constants have to be determined by a calibration.

3.2 Quasi-wall shear stress

For the present experimental setup, a calibration of the MHFS array was not performed. So, only qualitative values for the wall shear stress are provided by the hot-film sensors. In order to provide at least semi quantitative values for τ_w and thus enable a physical interpretation of the measurement results of the MHFS array with respect to the boundary layer, the quasi-wall shear stress τ_q as introduced by Hodson [18] and Hodson et al. [21] is used.

Based on Eq. (5), the constant B is replaced by the zero voltage U_0 of the hot-film sensors. From Eq. (4) it follows, that B^2 is related to the heat transfer or heat lost from the sensor to the substrat. Hodson [18] argues that $\dot{Q}_S$ is approximately equal to ${U_0}^2$ and thus $B \sim U_0$. As in general the total heat flux without inflow is a combination of heat loss to the substrate and free convection to the fluid, this argumentation is not very plausible. Rather, the wall shear stress must be zero if there is no inflow. Consequently, Eq. (5) must also become zero for that condition. As $A \neq 0$ and ΔT will not go to infinity, for practical reasons, the only way to satisfy this is $U(t)^2 - B^2 = 0$. Since $U(t) = U_0$ without flow, $B^2 = {U_0}^2$.

Furthermore, $\dot{Q} \sim \Delta T$ generally applies. This means, that $\dot{Q}_F$ is proportional to the temperature difference between the heated hot-film and the fluid and $\dot{Q}_S$ is proportional to ΔT related to the temperature of the substrate, so the wind tunnel model. If it is assumed that the model temperature coincides with the ambient air temperature, which will normally be the case, $U(t)^2 = R_S\,(\dot{Q}_F + \dot{Q}_S) \sim \Delta T$ follows according to Eq. (3), hence without inflow $\Delta T \sim {U_0}^2$. Thus the wall shear stress Eq. (5) can be approximated by the semi-quantitative representation

$$\tau_w \sim \tau_q = \left(\frac{U(t)^2 - {U_0}^2}{{U_0}^2} \right)^3 , \tag{6}$$

as it was used by Hodson et al. [21]. The so called quasi-wall shear stress τ_q has various advantages. On the one hand τ_q is proportional to the real wall shear stress, so it can be interpreted in a similar manner, which is shown below. On the other hand, also without calibration, it is possible to compare the signals of the hot-films with each other. In addition to the adjustment of the bridge, the normalization of each individual sensor with the associated zero voltage ensures that differences in the DC component of the respective bridges are not significant. Thus the respective bridge voltages $U(t)$ can be compared with each other, as it is done with the quasi-wall shear stress, rather than only the AC voltage components after deducting the DC component.

3.3 Identification of Boundary Layer Transition and Separation

To identify the state of the boundary layer, especially boundary layer transition and boundary layer separation like laminar separation bubbles, the wall shear stress

$$\tau_w = \eta \left. \frac{\partial u}{\partial y} \right|_{y=0} , \tag{7}$$

with the dynamic viscosity η can be used. τ_w is proportional to the gradient of the velocity profile $u(y)$ of the boundary layer at the wall, which is changed by a laminar-turbulent transition or a separation. So the wall shear stress shows a characteristic behavior for a boundary layer, which undergoes transition. This trend is schematically sketched in Fig. 3(a). Starting from a laminar boundary layer, the boundary layer thickness δ increases with increasing running length x. Therefore, the velocity gradient close to the wall decreases. Thus, the wall shear stress initially decreases with increasing laminar boundary layer thickness. As boundary layer transition occurs, δ grows significantly. In comparison with a laminar boundary layer, the flow velocities directly above the surface are significantly higher due to the strong mixing in the turbulent boundary layer. Since the no-slip condition is still satisfied, there is a small viscous sublayer with a velocity gradient near the wall that is strongly increased, resulting in high values of τ_w. The growth of the boundary layer and the viscous sublayer again lead to a reduction of the wall shear stress with increasing x.

While the boundary layer transition is combined with a separation, for example if a laminar separation bubble is formed, the near wall flow direction reverses, thus $\tau_w < 0$, as it is depicted in Fig. 3(b). Therefore, the

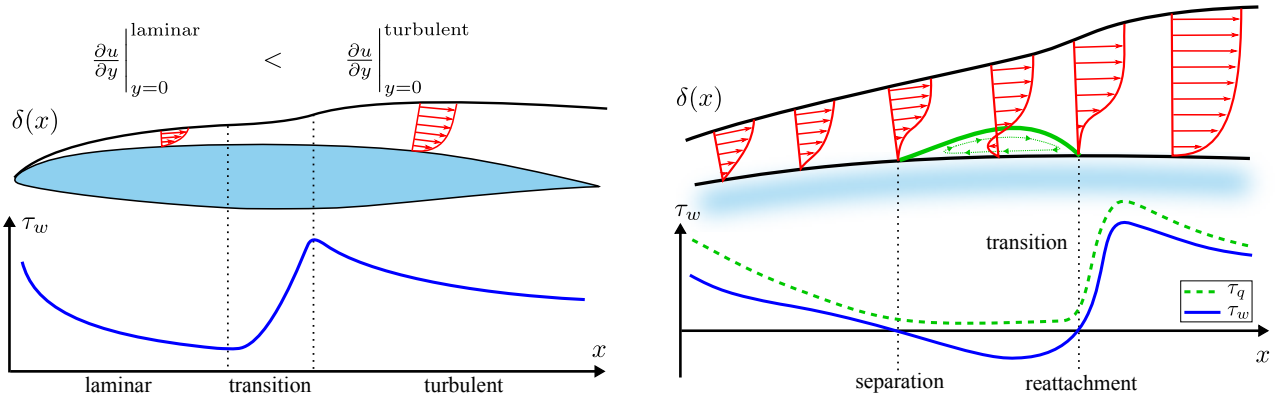

(a) $\tau_w(x)$ for a laminar-turbulent transition

(b) $\tau_w(x)$ for a laminar-turbulent transition with flow separation

Fig. 3 Trend of the wall shear stress for a laminar-turbulent boundary layer transition (a) and trend for a transition in combination with a laminar separation bubble (b). The wall normal direction is marked with y, the boundary layer thickness δ is greatly increased for purposes of clarification. For comparison, the green dotted line in (b) shows the schematic trend of the measured quasi-wall shear stress. The figure above in (b) is based on Roberts [22].

wall shear stress drops as the laminar boundary layer becomes unstable and is getting negative since the laminar boundary layer separates. τ_w then gets positive again and increases, as a turbulent boundary layer reattachment has taken place due to a transition from laminar to turbulent of the separated shear layer.

Since $\tau_w \sim \tau_q$, as given in Eq. 6, the trend of τ_q approximately follows the trends of τ_w, as shown in Fig. 3(b). Thus, a significant increase of τ_q indicates a laminar-turbulent transition of the boundary layer, whereas the strength of the increase still allows indications regarding the cause of the transition. This is particularly the case if the boundary layer undergoes a transition due to a compression shock. The strong pressure rise leads to a rapid transition and thus to a fast increase of τ_q, whereas a longer transition process leads to a slower one. However, this also depends on the extent to which the shock position corresponds to the position of a hot-film sensor, which can lead to a large variation in the signal magnitude.

A separation of the boundary layer is theoretically also indicated by a zero crossing and a negative value of τ_q. Since the hot-film sensors are not sensitive to a flow direction, detached areas with unsteady velocity profiles and strongly fluctuating flow directions also lead to an increased heat transfer compared to the zero state. So, in general the quasi-wall shear stress will be greater than zero. Nevertheless, areas in which τ_q is close to zero provide a strong indication of a separation of the boundary layer, as it is depicted by the green dotted line in Fig. 3(b).

In total, τ_q enables a physically justified identification of the boundary layer states, thus also a localization of transition and separation of the boundary layer, as it is carried out in the following paragraphs for the laminar airfoil experiments.

3.4 Data processing

During the wind tunnel experiments of a single day the facility warms up. As a result, the hot-film sensors are exposed to different ambient temperatures T_a during a series of measurements, hence the temperature difference ΔT varies. In order to ensure comparability of the measurements, the measured voltage signals $U(t)$ of the CTA anemometers are corrected. The correction formula

$$U_{\text{corr}} = U(t) \cdot \sqrt{\frac{T_S - T_0}{T_S - T_a}} \tag{8}$$

specified by Hultmark and Smits [23] is used for this, whereby it is assumed that changes in the flow properties due to the temperature change are negligible. The reference temperature T_0 is the temperature related to the last overheat set-up of the MHFS array. For further data analyses, the voltage signals U_{corr} are converted into quasi-wall shear stresses τ_q using Eq. 6. The zero voltages U_0 required for this are also corrected beforehand.

For steady measurement series, the sensor signals were recorded over a period of nearly 17 seconds. So, after the data processing described above, the signals are time-averaged to obtain $\bar{\tau}_q$. To quantify the fluctuation margin, the standard deviation and the minimum and maximum values are also calculated. The latter values are estimated by the mean values of the envelopes of the time series, which are obtained by identifying the peaks and smoothing over 1000 neighboring local maximums or minimums. This method is used in order not to overestimate individual strong signal outliers which may represent electrical and thus non-physical distortions.

In the case of unsteady measurements, the calculated time series of the quasi-wall shear stress are considered directly. An ensemble averaging of the MHFS signals over several oscillation periods, as it is carried out by Hodson et al. [21] etc., is usually not advisable due to the varying amplitudes during flutter and also with LCOs.

An at least rough localization of the boundary layer transition x_{tr} can be done by calculating the spatial gradient $\tau_q{}'$ of the quasi-wall shear stress along the chord x and an identification of the maximum, thus

$$\tau_q{}' = \frac{\partial \tau_q}{\partial x} \quad \Rightarrow \quad x_{tr} \approx \max(\tau_q{}') \; . \tag{9}$$

It should be noted that only the strongest increase of $\tau_q(x)$ is detected by Eq. 9, which generally correlates with the laminar-turbulent boundary layer transition as can be seen in Fig. 3(a) and Fig. 3(b). However, the spatial extent of the transition is not considered. Furthermore, it must be taken into account that an incorrect transition localization can be the result if first a transition and further downstream a compression shock occurs, maybe in connection with a turbulent separation of the boundary layer. This results in a first increase of the quasi-wall shear stress, which correlates with the transition, followed by a significant decrease and a renewed strong increase due to separation and shock. The maximum of $\tau_q{}'$ then occurs in conjunction with the shock and the position of the boundary layer transition x_{tr} is incorrectly detected. If this happens, a manual correction for x_{tr} can be made for steady series of measurements. An automated correction procedure for unsteady measurement series with large amounts of data is described in 4.2. Nevertheless, τ_q together with Eq. 9 provides an efficient way to detect particularly unsteady transition movements like those that occur with LCOs and thus provide important information concerning the unsteady aerodynamics of the laminar airfoil.

4 Results

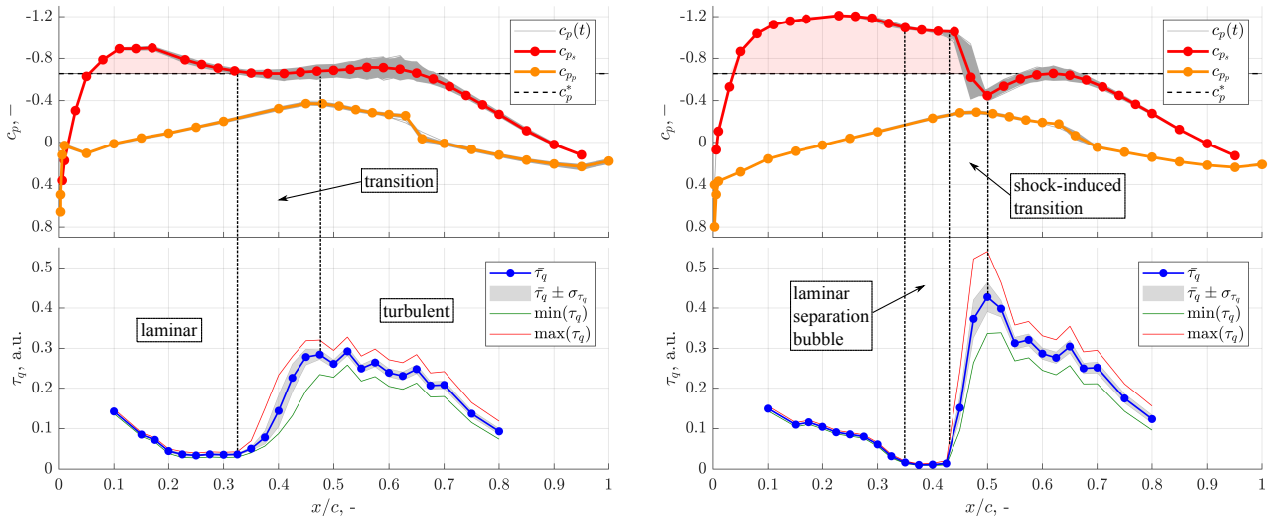

(a) Ma = 0.73 and $\alpha \approx 0°$

(b) Ma = 0.73 and $\alpha \approx 1.2°$

Fig. 4 Pressure distributions c_p (c_{p_s} corresponds the suction side and c_{p_p} to the pressure side of the laminar airfoil) and trend of the quasi-wall shear stress τ_q for a free boundary layer transition (a) and due to shock-boundary layer interaction (b). The red highlighted areas indicate supersonic regions, $c_p{}^*$ denotes the critical pressure coefficient and $c_p(t)$ the superposition of the measured time series for c_p. To resolve the fluctuations of τ_q, in addition to the temporal average $\bar{\tau}_q$, the standard deviation $\bar{\tau}_q \pm \sigma_{\tau_q}$ as well as the minimum and maximum values are plotted.

In this section results of the evaluation of the MHFS array signals for steady and unsteady measurements are presented. First, the boundary layer behavior for the fixed mounted laminar airfoil, so for steady flow is considered. In the following, an unsteady case is analyzed in which the laminar airfoil model performs a 1-DOF LCO in pitch. In this context, the estimation of the movement of the laminar-turbulent boundary layer transition depending on the motion of the airfoil itself is of great interest. At last, the unsteady transition in combination with the interaction of a compression shock during the LCO is summarized and discussed from the described results.

4.1 Boundary layer transition on the steady airfoil

The steady hot-film results were obtained prior to the flutter tests by measuring the lift and moment curves $c_l(\alpha)$ and $c_m(\alpha)$ of the laminar airfoil presented in Braune and Hebler [6]. The measurements were conducted at different Mach numbers for a Reynolds number of about $\mathrm{Re} \approx 2 \cdot 10^6$ for these cases. To get an impression of how the quasi-wall shear stress reflects boundary layer transition and laminar separation bubbles, two representative measuring points for a Mach number of $\mathrm{Ma} = 0.73$ are chosen. For this purpose, the pressure distribution and the measured quasi-wall shear stress on the airfoil's suction side are depicted in Fig. 4.

The first case, which is shown in Fig. 4(a) corresponds to an angle of attack of $\alpha \approx 0°$. No shock is formed and the boundary layer transition coincides with a slowly rising pressure gradient. As it is shown by the pressure distribution, the pressure gradient becomes positive behind $x/c \approx 0.2$. This results in a destabilization of the boundary layer, which leads to a laminar-turbulent boundary layer transition afterwards. Before the transition begins, the value of the quasi-wall shear stress is small, but clearly greater than zero. The trend does not indicate a separation of the boundary layer. The transition process itself is indicated by an increase of the quasi-wall shear stress, starting roughly at $x/c \approx 0.33$ and ends at $x/c \approx 0.48$. Before and after the transition τ_q decreases, as the theoretical development of the real wall shear stress τ_w (see Fig. 3) suggests. With the start of the transition, the fluctuations as well as the minimums and maximums of the quasi-wall shear stress increase. The same can be seen in the pressure distribution by $c_p(t)$. On the one hand, this indicates the increase of unsteadiness within the boundary layer due to turbulent mixing, on the other hand, a minimal movement of the transition can already be detected for the steady case. This in turn leads to the apparent temporal fluctuation of the pressure distribution on the suction side of the laminar airfoil and vice versa.

The second case corresponds to $\alpha \approx 1.2°$, shown in Fig. 4(b). A pronounced supersonic area occurs downstream of the leading edge, which closes with a compression shock at $x/c \approx 0.45$. Directly before the shock, a laminar separation bubble forms around $x/c \approx 0.4$. In the pressure distribution of the airfoil's suction side $c_{p,s}$ a plateau appears in this area, where the pressure remains constant. The quasi-wall shear stress is close to zero, which strongly indicates a separation of the boundary layer, as already shown in Fig. 3(b). It should be noted that, as discussed by Roberts [22] and Lee et al. [24] among others, the pressure plateau is related to the laminar part of the separation bubble, whereas the turbulent part of the bubble lies behind the plateau and coincides with a pressure recovery. τ_q already increases at the end of the plateau of $c_{p,s}$, thus already indicating a reattached shear layer at that point. So, a clear spatial restriction of the laminar separation bubble on the basis of the pressure distribution or also on the basis of the quasi-wall shear stress is only possible to a limited extent and subject to uncertainty. The same applies to the boundary layer transition, which is located directly behind the separation bubble and induced by a compression shock. The shock-boundary layer interaction leads to a strong and fast increase of τ_q. As before, pronounced fluctuations of τ_q occur. These are mainly due to a shock motion, as can be seen in the pressure distribution by $c_p(t)$. Furthermore, the high values of $\max(\tau_q)$ indicate, that the shock position partially coincides directly with the position of a hot-film sensor, leading to large amplitudes of τ_q. Both, the laminar separation bubble as well as the transition of the boundary layer in connection with a compression shock are therefore strongly correlated.

However, in both cases shown in Fig. 4, the boundary layer transition is indicated by a significant increase of the quasi-wall shear stress, which is steep in the case of a shock-induced transition. The latter is usually accompanied by a laminar separation bubble, for which τ_q falls to values close to zero in this range. So, it is shown that boundary layer transition and boundary layer separation can be read from the quasi-wall shear stress, even if a more accurate localization is limited by the resolution of the MHFS array.

To illustrate the influence of the angle of attack with respect to the boundary layer state in a broader range,

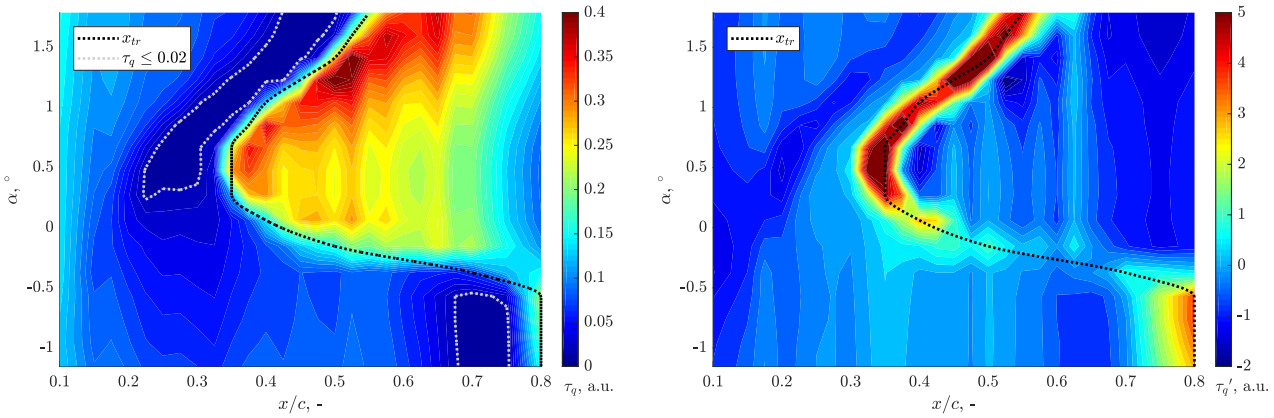

(a) $\tau_q(x/c,\alpha)$ for Ma = 0.73

(b) $\tau_q'(x/c,\alpha)$ for Ma = 0.73

Fig. 5 Distribution of the quasi-wall shear stress $\tau(x/c,\alpha)$ (a) and the spatial gradient $\tau_q'(x/c,\alpha)$ (b) for Ma = 0.73. The trend of the boundary layer transition based on the gradient maximum as well as areas indicating a boundary layer separation ($\tau_q \leq 0.02$) are marked.

$\tau_q(x/c)$ against α is plotted in Fig. 5(a) for Ma = 0.73. This Mach number is chosen because the laminar airfoil experienced 1-DOF LCOs in pitch for these flow conditions [6]. For the reason of clarity, the quasi-wall shear stress is presented by color coded contour plots. Besides the quasi-wall shear stress, the spatial gradient $\tau_q'(x/c,\alpha)$ is shown in Fig. 5(b). This was calculated in order to localize the laminar-turbulent boundary layer transition, as already mentioned. The transition is marked by a black dotted line in Fig. 5, based on an estimation of x_{tr} by Eq. 9. Furthermore, areas in which $\tau_q \leq 0.02$ applies are marked by a gray dotted line. Although this is an empirically determined value, these areas indicate a separation of the boundary layer, i.e. the formation of a laminar separation bubble.

As can be seen in Fig. 5, a significant movement of the transition occurs by varying the angle of attack, which is directly related to the characteristic laminar bucket of the airfoil. This appears in the drag polar shown in Fig. 6. For low α, the transition is near the trailing edge and correlates with a strong pressure increase in

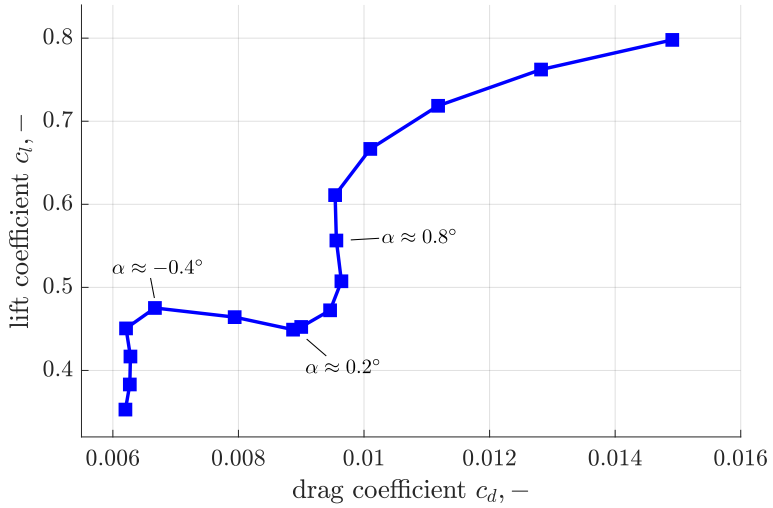

Fig. 6 Drag polar for the laminar aifoil model for Ma = 0.73, based on Braune and Hebler [25]. The angles of attack at which the flow changes significantly are marked.

the range $x/c \approx 0.75$, which destabilizes the boundary layer. Upstream of this pressure increase, the low values of τ_q indicate a laminar separation bubble, which is marked in Fig. 5(a). An increase of α then leads to a rapid movement of the boundary layer transition upstream. This starts at an angle of attack of about $-0.4°$

and correlates with the beginning of the drag plateau in Fig. 6. The transition moves up to $x/c \approx 0.35$ to the leading edge, where it can be located almost constantly in an angle of attack range of $0.2° \lesssim \alpha \lesssim 0.8°$. For larger angles the transition moves downstream again, where it correlates with a compression shock. This leads to the increased values of the quasi-wall shear stress behind the transition line in Fig. 5(a) as well as to the large gradients which can be seen in Fig. 5(b). The shock-boundary layer interaction starts at $\alpha \approx 0.2°$, thus the transition is shock-induced beyond this point. This correlates approximately with the end of the drag plateau marked in Fig. 6. So, as the shock starts to move downstream, the transition moves downstream as well. Furthermore, the shock-induced transition takes place in interaction with a laminar separation bubble, which is marked as previously in Fig. 5(a).

Regarding the behavior of the boundary layer during a 1-DOF LCO around $\alpha_0 \approx 0°$ with measured amplitudes of $|\Delta\alpha| \approx 0.7°$ for $\mathrm{Ma} = 0.73$ [6], the steady results already show a significant movement of the transition location as well as the occurrence of laminar separation bubbles within these angle of attack range. x_{tr} moves in a range of $0.35 \lesssim x/c \lesssim 0.75$ within the observed LCO amplitudes. The strong variation of the boundary layer in combination with a shock-boundary layer interaction results in a pronounced nonlinear aerodynamic behavior of the laminar airfoil as already described in Braune and Hebler [6], which can also be clearly recognized by the drag polar in Fig. 6. This complex aerodynamics represents the cause for the occurrence of the observed 1-DOF LCOs. In particular, the unsteady boundary layer behavior therefore requires more detailed investigation, as presented below.

4.2 Boundary layer transition during LCO

In the case of an unsteady flow, as present during a LCO, strong changes occur within the boundary layer depending on the airfoil's motion. In order to discuss the behavior of the boundary layer while the laminar airfoil is performing 1-DOF LCOs in pitch, a direct analysis of the temporal development of the quasi-wall shear stress is carried out. For this a representative LCO is selected, for which the behavior of the aerodynamic forces $c_l(t)$ and $c_m(t)$ as well as the change of the pressure distribution over an oscillation period of the LCO have already been discussed in detail in Braune and Hebler [6]. The LCO is shown in Fig. 7, which has occurred at a stagnation pressure of 55 kPa, a Mach number of $\mathrm{Ma} = 0.73$ and an angle of attack of $\alpha_0 \approx 0°$. The LCO

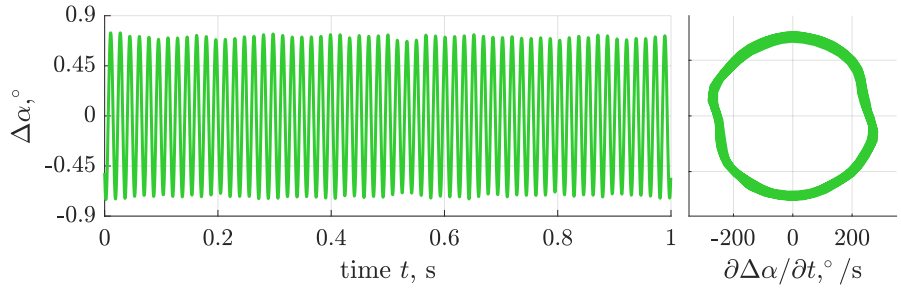

Fig. 7 Time series and phase space representation of a LCO in pitch of the laminar airfoil model.

has an amplitude of $|\Delta\alpha| \approx 0.72°$ and a reduced frequency of $\omega^* = \omega_\alpha c/u_\infty \approx 0.46$. For the same time period regarded in [6], the quasi-wall shear stress $\tau_q(x/c,t)$ and the gradient $\tau_q{}'(x/c,t)$ are shown for three oscillation periods in Fig. 8. For convenience, only every 50 data point of the hot-film signals were used, which provides sufficient time resolution due to the very high sampling rate of the MHFS array. As before, the quasi-wall shear stress and the gradient are represented by color-coded contours. Fig. 8 shows that the periodic motion of the model during a LCO also produces a periodic behavior of the boundary layer. A pronounced movement of the laminar-turbulent boundary layer transition occurs as well as a periodic formation of laminar separation bubbles. The transition line $x_{tr}(t)$ and areas in which $\tau_q < 0.02$ are marked again, equivalent to the steady case. However, estimating the transition position $x_{tr}(t)$ is more complex for the unsteady case. The direct evaluation of $\tau_q(x/c,t)$ and the large amount of data associated with it, leads to an increased number of incorrect transition positions, as previously mentioned in 3.4.

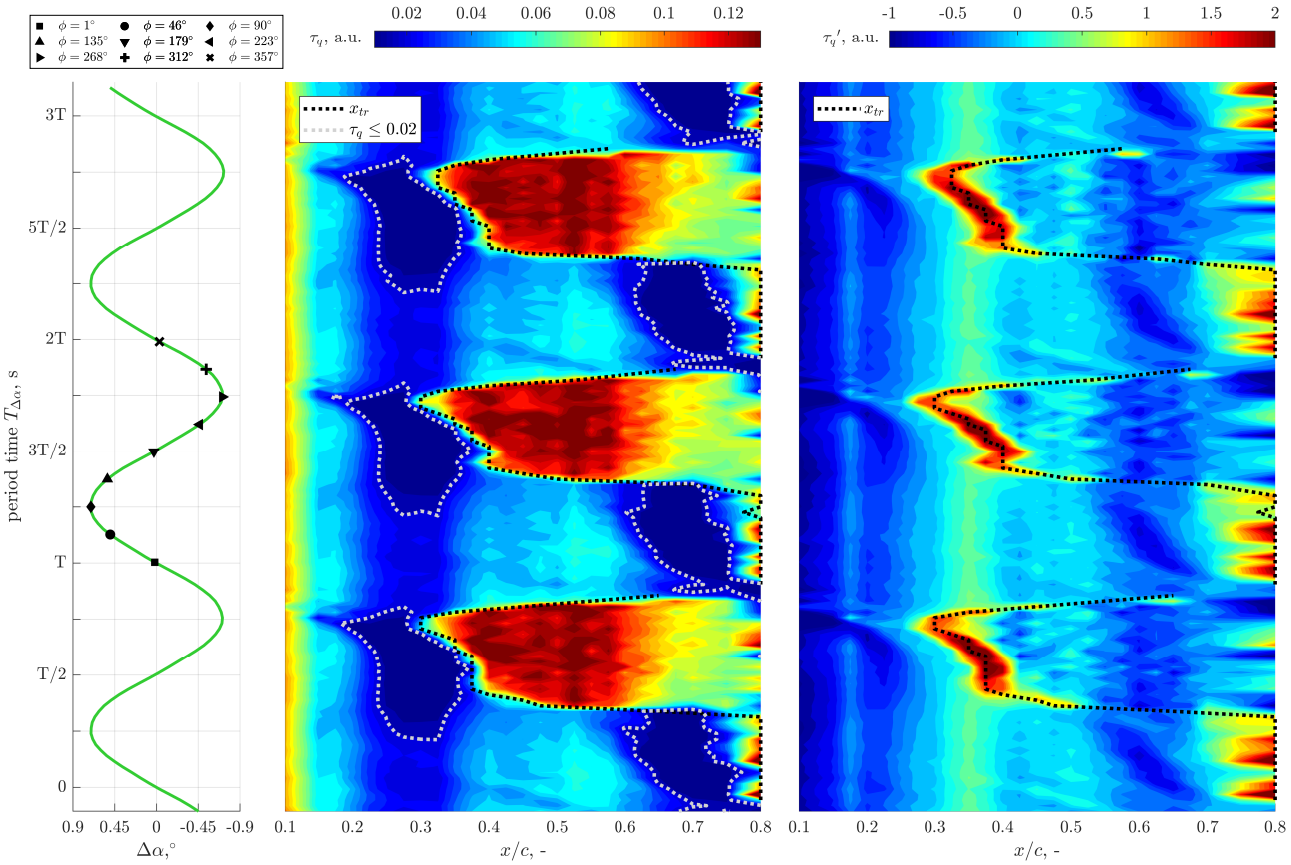

Fig. 8 Temporal and spatial development of the quasi-wall shear stress $\tau_q(x/c,t)$ and the spatial gradient $\tau_q(x/c,t)'$ on the suction side of the laminar airfoil during a LCO. As before, regions indicating a laminar separation bubble ($\tau_q \leq 0.015$) and the detected transition line x_{tr} are depicted.

In order to perform an automated detection and marking of the boundary layer transition, a three-stage algorithm is applied for the estimation of $x_{tr}(t)$. In the first step, the maximum of the gradient $\tau_q{}'(x/c,t_i)$ is calculated for each time point t_i according to Eq. 9. The transition position determined in this way is shown by the red dotted line in Fig. 9 for the regarded time segment of the LCO. As can be seen, sometimes outliers appear in $x_{tr}(t)$ during a period (marked regions 1 in Fig. 9). Supposedly, the transition here seems to jump abruptly from $x/c \approx 0.8$ upstream to $x/c \approx 0.35$ and back again or during the movement downstream it moves again briefly towards the leading edge before jumping to $x/c \approx 0.8$. In this marked regions 1, no transition occurs within the sensor range. The quasi-wall shear stress thus shows no significant increase, whereas slight increases of τ_q, on the other hand, are incorrectly interpreted as transition in the first step. This is avoided in the second step where, in addition to the necessary condition according to Eq. 9, the sufficient condition $\tau_q(x/c \geq 0.2,t_i) \geq \tau_{q,l}$ is introduced. If at the time t_i no quasi-wall shear stresses along the sensor range behind $x/c = 0.2$ reach or exceed an empirically defined threshold value $\tau_{q,l}$, no transition is detected. For the presented case, the threshold is set to $\tau_{q,l} = 0.065$. The thus estimated transition position is illustrated by the blue dashed curve in Fig. 9. Corresponding areas (marked regions 1 in Fig. 9) are therefore omitted, as can be seen. The third step is to correct incorrect transition positions due to a shock-boundary layer interaction with more than one occurring compression shock. This would be the case, for example, with a double-shock system, as it occurs on the laminar airfoil for slightly higher Mach numbers than those shown here. The boundary layer transition is induced by the first shock more upstream, whereas the second shock or at least a significant increase in pressure downstream can lead to a new signal rise of the hot-films and thus of τ_q, if shock and sensor position coincide. Therefore, the second increase of τ_q can be misinterpreted as a transition position, leading to isolated discontinuities of x_{tr}. Although these are physically justified, they are not related to the laminar-turbulent boundary layer transition and must be filtered out by the transition detection algorithm. Since these can be treated as statistical outliers, so to speak, they are filtered with a median filter. It should be noted

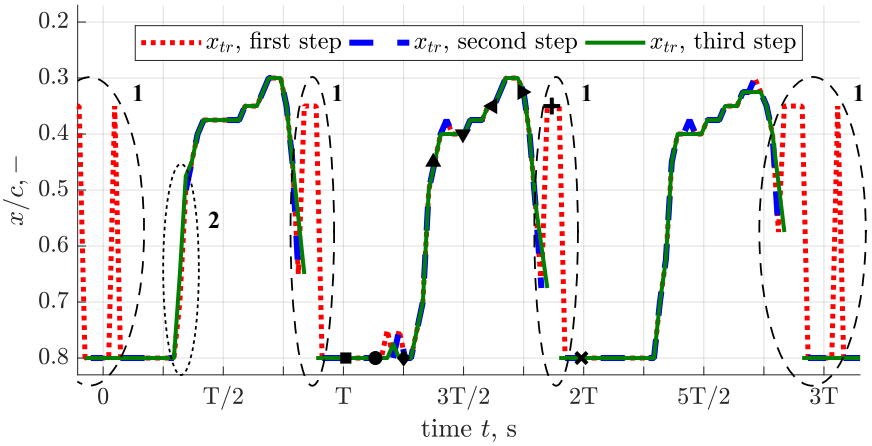

Fig. 9 Representation of the individual steps for the transition detection of unsteady measurements for the regarded time section of the LCO. The phase angles are marked as well.

that the window length of the median filter should be as small as possible to achieve reliable outlier suppression but avoid significant signal suppression. Furthermore, a too large window size leads to a phase distortion of x_{tr}. However, the remaining marked region 2 in Fig. 9 corresponds to a detected transition in the first step, but is omitted in the second step as the quasi-wall shear stress does not exceed values above $\tau_{q,l}$ in this region. In the context of the temporal consideration of the boundary layer movement, such deviations from the periodicity, i.e. supposedly short interruptions in the boundary layer transition, as in region 2, occur only very sporadically in the course of the entire time series. These regions can also be considered as statistical outliers, without receiving a greater physical weight, and are therefore also captured and corrected by the median filter. The final estimated position of the transition is depicted in Fig. 9 by a green curve. Ultimately, the algorithm allows time resolved detection of the laminar-turbulent boundary layer transition as shown in Fig. 8.

Nevertheless, in order to obtain a precise overview of the behavior of the boundary layer during the presented LCO, nine phase angles ϕ were marked for one oscillation period in Fig. 8. The phase angles are selected so that an increment of approximately $\Delta\phi \approx 45°$ is achieved. For the corresponding times t_{ϕ_i} the respective trend of the quasi-wall shear stress $\tau_q(x/c, t_{\phi_i})$ is shown individually in Fig. 10. Furthermore, the corresponding distributions of the pressure coefficient of the suction side of the laminar airfoil $c_{p,s}$ are depicted, which have already been discussed in [6].

Starting with a phase angle of $\phi = 1°$, during the upward movement of the model there is only a slight change in the boundary layer and the pressure distribution until the amplitude maximum at $\phi = 90°$ is reached. For all three phase angles, τ_q begins to rise in the range $0.3 \lesssim x/c \lesssim 0.4$. This may indicate an onset of boundary layer transition and correlate with an increase in pressure, suggesting destabilization of the boundary layer. Behind $x/c \approx 0.4$ there is again a pressure drop and thus an acceleration of the flow which again leads to a stabilization of the boundary layer. In fact, the boundary layer transition is shock-induced for all three phase angles. During the upstroke of the laminar airfoil, the compression shock moves from nearly $x/c \approx 0.8$ for $\phi = 1°$ to $x/c \approx 0.75$ for $\phi = 90°$. The transition also moves upstream accordingly, but this is not detected by the spatially limited resolution of the MHFS array and therefore also not detected by the transition detection algorithm. Thus a transition position of $x/c = 0.8$ is estimated for all three phase angles, which is marked by grey vertical lines in Fig. 10, the black dotted line in Fig. 8 and, in addition, can be seen in Fig. 9. Furthermore, for all three phase angles, a laminar separation bubble occurs before the shock or transition in the range of approximately $0.65 \lesssim x/c \lesssim 0.75$. This can be seen both in the pressure distribution and the trend of the quasi-wall shear stress. The bubble moves slightly upstream as the phase angle increases, as indicated by the shapes of the marked regions ($\tau_q \leq 0.02$) in Fig. 8. Thus a laminar boundary layer is present for the entire upstroke movement of the laminar airfoil up to $x/c \approx 0.65$.

As the downstroke of the laminar airfoil begins, the laminar running length shortens abruptly and the transition moves very quickly upstream. A pronounced supersonic area forms in the front area of the airfoil

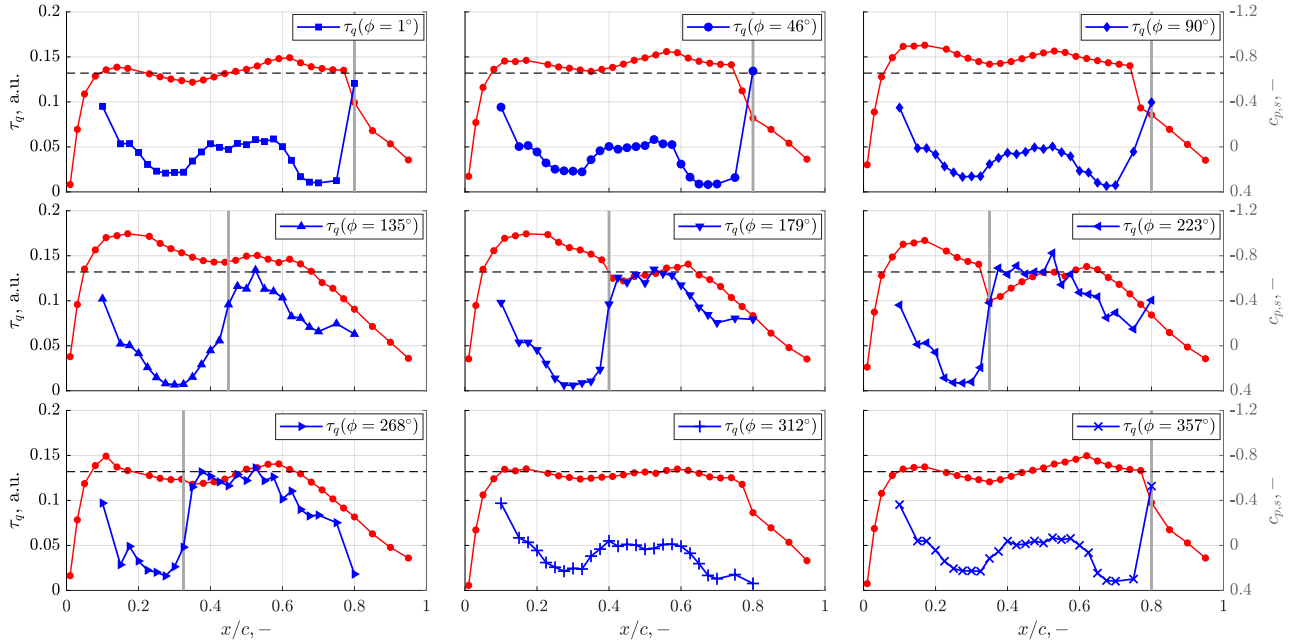

Fig. 10 Quasi-wall shear stress $\tau_q(x/c, t_{\phi_i})$ (blue line) and pressure distribution $c_{p,s}$ (red line) for the phase angles marked in Fig. 8 of one oscillation period of the investigated LCO. The black dotted line marks the critical pressure coefficient c_p^*, the gray line marks the position of the transition x_{tr}, estimated by the algorithm.

model, which is attenuated by a pressure increase within the range $0.2 \lesssim x/c \lesssim 0.4$ for $\phi = 135°$. This induces the boundary layer transition without a compression shock occurring. The transition position is $x_{tr} \approx 0.45\ c$. In the further progress, the supersonic area closes again with a compression shock, which induces the transition. Thus the shock and transition position for $\phi = 179°$ and $\phi = 223°$ correlate with $x_{tr}(\phi = 179°) \approx 0.4\ c$ and $x_{tr}(\phi = 223°) \approx 0.35\ c$, respectively. The movement of the shock upstream therefore also leads to an upstream movement of the laminar-turbulent boundary layer transition, which can be clearly seen in Fig. 8. Furthermore, a comparison of $\phi = 1°$ with $\phi = 179°$ shows the influences of the unsteady flow or the model motion. Although the quasi-steady angle of attack is identical in both cases, the pressure distribution and the trend of the quasi-wall shear stress differ significantly from each other. This is discussed in more detail in 4.3. In the case of the shock-induced transition for $\phi = 179°$ and $\phi = 223°$ a laminar separation bubble occurs again prior to the shock. The same is indicated by τ_q for $\phi = 135°$, whereas the pressure distribution does not show the characteristic plateau, thus no unambiguous identification of a separation bubble is possible. In the amplitude minimum of the LCO at $\phi = 268°$ the pronounced supersonic area has largely disappeared. The transition here is again related to an increase in pressure. The transition position is $x_{tr} = 0.325\ c$, which means that the laminar airfoil has the shortest laminar running length during a LCO period.

The renewed upstroke of the laminar airfoil model leads to a nearly constant trend of the pressure distribution along c_p^* for $\phi = 312°$. As a result, no transition occurs over the entire range of the hot-film sensors. Due to the second step of the algorithm for transition detection, no transition is localized here either, as it is shown by the marked region (2) in Fig. 9. For $\phi = 357°$ an shock occurs again at $x/c \approx 0.8$, which induces a transition. The periodicity of the boundary layer behavior during the LCO, as it is clearly obvious from Fig. 8, leads to an approximately identical flow field as for $\phi = 1°$.

Altogether it is shown that in the progress of an LCO period within a change of the phase angle of only $\Delta\phi \approx 45°$ a very large motion of the transition occurs from $x_{tr} = 0.35\ c$ in the amplitude minimum to outside of the sensor range $x_{tr} > 0.8\ c$, if one occurs at all. In order to obtain a relationship between model motion and boundary layer transition, the detected transition position $x_{tr}(x/c, t)$ is plotted together with the pitch motion of the airfoil in Fig. 11. With regard to the aeroelastic stability and a further analysis of the unsteady aerodynamics of the laminar airfoil, the phase lag between $\Delta\alpha$ and $x_{tr}(x/c, t)$ is of interest. For a basic definition of a phase difference, a linear relationship between angle of attack motion and transition motion is assumed for

simplification, even though this is not valid for the laminar airfoil as Fig. 5(a) and 5(b) show. Nevertheless, a spectral decomposition of the transition motion has been performed and the first harmonic of $x_{tr}(x/c,t)$, which has the same frequency as the model motion, is filtered out (red line in Fig. 11). Thus, a phase difference

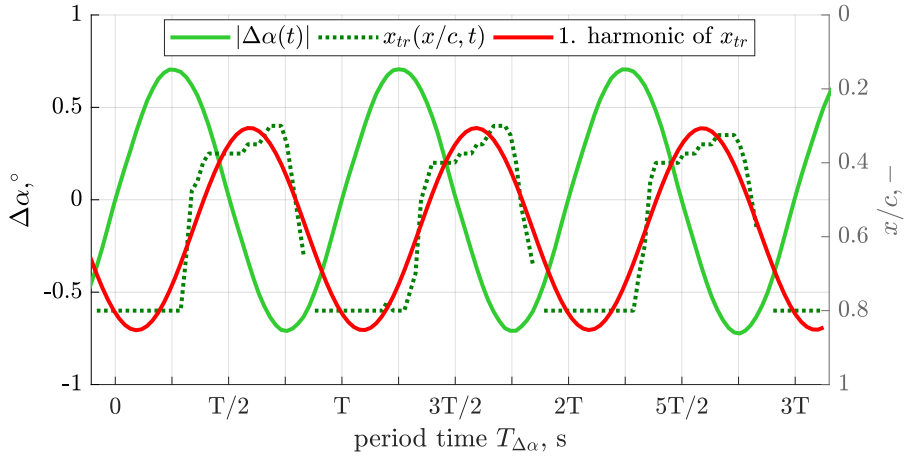

Fig. 11 Comparison of the model motion with the movement of the transition position represented by the first harmonic component of $x_{tr}(x/c,t)$.

between the model motion and the transition of $\Delta\varphi \approx -121°$ can be estimated by calculating the transfer function. It can thus be seen that the transition movement significantly lags behind the model motion.

This large phase difference, on the one hand, quantifies the influence of the unsteady flow or model motion concerning the boundary layer behavior, which can already be seen by a direct comparison of the steady and unsteady observations for Ma = 0.73 in Fig. 5 and Fig. 8, respectively. On the other hand, this phase shift also has a significant influence on the aerodynamic forces and in particular on the aerodynamic moment, which has a comparable phase difference to the model movement [6]. This influence can be illustrated as a kind of additional camber effect due to the thickening of the boundary layer by the boundary layer transition. Since the influence of the free transition on the aeroelastic stability of the laminar airfoil has already been confirmed by Hebler [2] and especially the influence of the occurrence of 1-DOF LCOs by Braune and Hebler [6], it is obvious that the delayed boundary layer response to the model motion plays a significant role in the mechanism behind the 1-DOF LCOs of the laminar airfoil.

4.3 Unsteady shock-boundary layer interaction during LCO

The evaluation of the signals of the MHFS array in combination with the investigation of the pressure distributions [6] shows that the unsteady aerodynamics of the laminar airfoil, experiencing a 1-DOF LCO, is dominated by a unsteady shock-boundary layer interaction. On the one hand a type B shock motion according to Tijdeman and Seebass [26] and on the other hand a periodic movement of the boundary layer transition occurs. The latter has similarities to the shock motion in that it leads to an interrupted boundary layer transition, so to speak to a type B transition. To summarize this complex behavior, the results obtained are schematically illustrated for one LCO period in Fig. 12.

As it shows, two distinct areas occur where the boundary layer transition is shock-induced. During the upstroke movement ($0 \leq \phi \leq \frac{\pi}{2}$), a shock occurs in the rear quarter of the laminar airfoil, which performs an inverse shock motion and moves minimally towards the leading edge. Schewe and Mai [27] argue that this provides an indication of a detachment of the boundary layer behind the shock, i.e. a trailing edge separation that moves upstream. The boundary layer transition is connected to the shock and therefore also moves minimally to the leading edge, as well as the occurring laminar separation bubble. An abrupt change in the boundary layer occurs with the reversal of the direction of motion of the laminar airfoil, so after $\max(\Delta\alpha)$ is reached.

With the start of the downstroke ($\phi = \frac{3}{4}\pi$) the boundary layer transition jumps forward to $x/c \approx 0.45$ and continuously moves upstream up to $x/c \approx 0.325$ for $\phi = \frac{3}{2}\pi$. For $\pi \leq \phi \leq \frac{5}{4}\pi$ a shock region is formed at

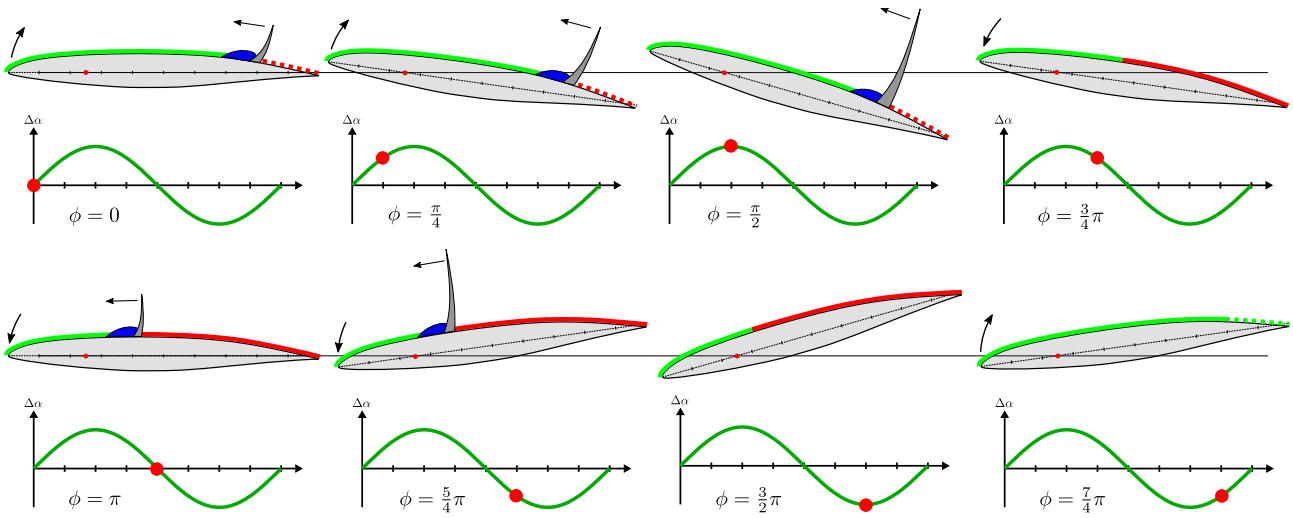

Fig. 12 Schematic visualization of the movement of the laminar-turbulent boundary layer transition in connection with a shock motion and resulting shock-boundary layer interaction for one period of the regarded 1-DOF LCO of the laminar airfoil model. Laminar areas of the boundary layer are shown in green, whereas turbulent areas are shown in red. Laminar separation bubbles are visualized schematically in blue and shocks in grey. It is noted that behind $x/c = 0.8$ no boundary layer information is available anymore. The prevailing boundary layer states are therefore extrapolated to the trailing edge. A possible flow separation at this point is not considered.

$x/c \approx 0.4$, which induces the boundary layer transition and also moves upstream. The state of the boundary layer changes with a reversal of the direction of motion after reaching $\min(\Delta\alpha)$, as seen before.

For $\phi = \frac{7}{4}\pi$ no boundary layer transition can be detected within the resolution range of the sensors. The transition has therefore shifted by at least half the chord to the trailing edge. Only at the end of a full period ($\phi = 2\pi$ or $\phi = 0$) a transition, which is then shock-induced, can be localized again at $x/c = 0.8$.

Thus it is shown that a sudden movement of the boundary layer transition occurs especially in the upper and lower reversal point of the model motion. Furthermore, a shock-induced transition occurs during the upstroke and downstroke, after each zero crossing of $\Delta\alpha$. Both effects correlate with a strong change in the flow velocities induced by the motion or a related change in the local angle of attack. As a result of the 1-DOF motion of the laminar airfoil model in pitch about the axis of rotation at $c/4$, an upstroke motion can be interpreted as a reduction in the local angle of attack in front of $c/4$ and as an increase behind $c/4$. This local increase thus leads to an acceleration of the flow and consequently to a stabilization of the boundary layer. This results in a long laminar running length, which is present for the upstroke of the laminar airfoil. This process reverses accordingly as soon as the model executes a downstroke motion and consequently leads to an earlier boundary layer transition upstream. In addition to influencing the boundary layer transition, the induced velocities also influence the pressure distribution and thus the shock position, which in turn interacts with the boundary layer. These aspects also explain the large phase shift between model movement and boundary layer transition. Therefore, the conclusion is obvious that the observed effects are dependent on the LCO amplitude and especially on the LCO frequency, which is decisive for the induced velocities, in addition to the stationary flow field. A analysis of these relationships is the subject of further investigations.

5 Concluding remarks

This paper presented an investigation of the unsteady boundary layer transition and shock-boundary layer interaction on a CAST 10 supercritical laminar airfoil in transonic unsteady flow. CTA anemometry measurements of the boundary layer using an MHFS array were performed while the model experienced 1-DOF LCOs in pitch. The hot-film signals were evaluated on the basis of the physically motivated quasi-wall shear stress. The boundary layer states for both steady and unsteady flows were analysed, whereby in particular the laminar-turbulent boundary layer transition and laminar separation bubbles were resolved. A three-stage algorithm was developed, on the basis of which a detection of the transition is also possible during unsteady measurements and

occurring shock-boundary layer interaction. For the first time, this enabled a direct relationship to be derived and quantified between the model motion during a LCO and the movement of the boundary layer transition for transonic flow conditions.

In the steady case, the airfoil model shows a clear shift of the transition position for $\mathrm{Ma} = 0.73$ as a function of the angle of attack, which is directly related to the occurrence of a plateau in the drag polar, as it is characteristic for a laminar airfoil. Outside of this plateau a shock-boundary layer interaction was found where a laminar separation bubble occurs prior to the shock. Transition and shock position coincide for these angle of attack ranges.

In comparison to the unsteady boundary layer behavior and the position of the transition during a LCO, clear deviations to the steady case occur. A sudden movement of the boundary layer transition has been found in the upper and lower reversal point of the LCO, whereas a shock-induced transition in combination with a laminar separation bubble occurred in the last section of the upstroke and downstroke of the laminar airfoil. This is directly related to the locally induced velocities as a result of the unsteady flow or model motion, which lead to a delay and thus to a phase shift of $\phi \approx -121^\circ$ between the model motion and the movement of the laminar-turbulent boundary layer transition. The transition therefore lags behind, which in turn affects the aerodynamic forces and thus the aeroelastic stability of the laminar airfoil.

Some extensions and improvements can still be made regarding the evaluation of the hot-film signals. The theoretical principles on which the derivation of the quasi-wall shear stress is based are subject to some assumptions and simplifications. Especially in connection with the transonic flow local compressibility and temperature effects occur, which influence the heat transfer and thus the sensor signal. This is not taken into account here. However, it suggests that these effects are negligible with regard to an anyway purely qualitative interpretation of the quasi-wall shear stress. Concerning a temperature correction of the individual sensors, there are other temperature correction methods than those used in this work, which may be more accurate under the aspects mentioned above. The requirement of the temperature correction applied here was primarily an adjustment of the signals of different measuring points due to the warming of the wind tunnel. A more detailed local consideration of the temperature is recommended for further investigations. Finally, it should be noted that an interpolation of the sensor signals or the quasi-wall shear stress along the chord would lead to a higher spatial resolution accuracy of the transition position. The detected transition position is currently linked to a hot-film sensor position, so that smaller transition movements are not resolved, as is the case in Fig. 10 for $\phi = 1^\circ$ up to $\phi = 90^\circ$ for example. An interpolation leads to a higher number of spatial sampling points and consequently to a better resolution even of smaller changes of the transition position below the spatial resolution of the sensors.

However, the presented work successfully shows that on the basis of the evaluation methodology of the hot-films a largely automated detection of the unsteady boundary layer transition is possible, even under transonic flow and associated shock-boundary layer interaction. Ongoing work is now focused on establishing a connection between the delayed boundary layer response in conjunction with the occurring shock-boundary layer interaction and the energy input of the flow into the motion of the model. The aim is to more accurately identify the flow processes and conditions leading to the occurrence of 1-DOF LCOs and the associated aeroelastic instability of the supercritical laminar airfoil.

References

[1] L. Tichy, H. Mai, M. Fehrs, J. Nitzsche, and A. Hebler. Risk analysis for flutter of laminar wings. In *International Forum on Aeroelasticity and Structural Dynamics (IFASD), 25-28 June 2017, Como, Italy*, 2017.

[2] A. Hebler. Experimental assessment of the flutter stability of a laminar airfoil in transonic flow. In *International Forum on Aeroelasticity and Structural Dynamics (IFASD), 25-28 June 2017, Como, Italy*, 2017.

[3] A. C. L. M. van Rooij and W. Wegner. Numerical investigation of the flutter behavior of a laminar supercritical airfoil. In A. Dillmann, G. Heller, E. Krämer, H.-P. Kreplin, W. Nitsche, and U. Rist, editors,

New Results in Numerical and Experimental Fluid Mechanics IX, volume 124 of *Notes on Numerical Fluid Mechanics and Multidisciplinary Design*, pages 33-41. Springer, 2014.

[4] M. Fehrs. Influence of transitional flows at transonic mach numbers on the flutter speed of a laminar airfoil. In *International Forum on Aeroelasticity and Structural Dynamics (IFASD), 24-26 June 2013, Bristol, United Kingdom*, 2013.

[5] M. Fehrs, A. C. L. M. van Rooij, and J. Nitzsche. Influence of boundary layer transition on the flutter behavior of a supercritical airfoil. *CEAS Aeronautical Journal*, 6(2):291-303, 2015.

[6] M. Braune and A. Hebler. Experimental investigation of transonic flow effects on a laminar airfoil leading to limit cycle oscillations. In *2018 Applied Aerodynamics Conference, AIAA AVIATION Forum, 25-29 June 2018, Atlanta, Georgia*, 2018. doi: https://doi.org/10.2514/6.2018-3641.

[7] H. W. Liepmann and G. T. Skinner. Shearing-stress measurements by use of a heated element. Technical Note 3268, National Advisory Committee for Aeronautics, 1954.

[8] B. J. Bellhouse and D. L. Schultz. Determination of mean and dynamic skin friction, separation and transition in low-speed flow with a thin-film heated element. *Journal of Fluid Mechanics*, 24(2):379-400, 1966. doi: https://doi.org/10.1017/S0022112066000715.

[9] J. Leuckert, R. Erdmann, W. Nitsche, and H. Rosemann. On transition detection at high subsonic freestream mach numbers using thermoresistive surface sensors. In *49th AIAA Aerospace Sciences Meeting including the New Horizons Forum and Aerospace Exposition Orlando, Florida*, 2011. doi: https://doi.org/10.2514/6.2011-879.

[10] T. Lee and S. Basu. Measurement of unsteady boundary layer developed on an oscillating airfoil using multiple hot-film sensors. *Experiments in Fluids*, 25(2):108-117, 1998. doi: https://doi.org/10.1007/s003480050214.

[11] K. Richter, S. Koch, and A.D. Gardner. Influence of oscillation amplitude and mach number on the unsteady transition on a pitching rotor blade airfoil. In *AHS 69th Annual Forum, Phoenix, Arizona, May 21-23*, 2013.

[12] K. Richter, S. Koch, A.D. Gardner, H. Mai, A. Klein, and C.-H. Rohardt. Experimental investigation of unsteady transition on a pitching rotor blade airfoil. *Journal of the American Helicopter Society*, 59(1), 2014. doi: 10.4050/JAHS.59.012001.

[13] H. Mai and A. Hebler. Aeroelasticity of a laminar wing. In *International Forum on Aeroelasticity and Structural Dynamics (IFASD), 26-30 June 2011, Paris, France*, 2011.

[14] A. Hebler, L. Schojda, and H. Mai. Experimental investigation of the aeroelastic behaviour of a laminar airfoil in transonic flow. In *International Forum on Aeroelasticity and Structural Dynamics (IFASD), 24-26 June 2013, Bristol, United Kingdom*, 2013.

[15] K. Richter, S. Koch, A. Goerttler, B. Lütke, C. C. Wolf, and A. Benkel. Unsteady boundary layer transition on the dsa-9a rotor blade airfoil. In *41st European Rotorcraft Forum, Munich, Germany, 01.- 04. September*, 2015.

[16] K. Richter, C. C. Wolf, A. Gardner, and C. B. Merz. Detection of unsteady boundary layer transition using three experimental methods. In *54th AIAA Aerospace Sciences Meeting, 4-8 January, San Diego, California, USA*, 2016. doi: https://doi.org/10.2514/6.2016-1072.

[17] A. Goerttler, A.D. Gardner, and K. Richter. Unsteady boundary layer transition detection by automated analysis of hot film data. In A. Dillmann, G. Heller, E. Krämer, C. Wagner, S. Bansmer, R. Radespiel, and R. Semaan, editors, *New Results in Numerical and Experimental Fluid Mechanics XI*, volume 136 of *Notes on Numerical Fluid Mechanics and Multidisciplinary Design*, pages 387–395. Springer, 2017. doi: https://doi.org/10.1007/978-3-319-64519-3_35.

[18] H. P. Hodson. Boundary-layer transition and separation near the leading edge of a high-speed turbine blade. *Journal of Engineering for Gas Turbines and Power*, 107(1):127-134, 1985. doi: doi:10.1115/1.3239672.

[19] G. Dietz, G. Schewe, and H. Mai. Amplification and amplitude limitation of heave/pitch limit-cycle oscillations close to the transonic dip. *Journal of Fluids and Structures*, 22:505-527, 2006. doi: https://doi.org/10.1016/j.jfluidstructs.2006.01.004.

[20] L. V. King and H. T. Barnes. On the convection of heat from small cylinders in a stream of fluid: Determination of the convection constants of small platinum wires, with applications to hot-wire anemometry. In *Proceedings of the Royal Society of London. Series A, Containing Papers of a Mathematical and Physical Character*, 1914. doi: https://doi.org/10.1098/rspa.1914.0089.

[21] H. P. Hodson, I. Huntsman, and A. B. Steele. An investigation of boundary layer development in a multistage lp turbine. *Journal of Turbomachinery*, 116(3):375–383, 1994. doi: doi:10.1115/1.2929424.

[22] W. B. Roberts. Calculation of laminar separation bubbles and their effect on airfoil performance. *AIAA Journal*, 18(1):25-31, 1980. doi: https://doi.org/10.2514/3.50726.

[23] M. Hultmark and A. J. Smits. Temperature corrections for constant temperature and constant current hot-wire anemometers. *Measurement Science and Technology*, 21(10), 2010. doi: https://doi.org/10.1088/0957-0233/21/10/105404.

[24] D. Lee, S. Kawai, T. Nonomura, M. Anyoji, H. Aono, A. Oyama, K. Asai, and K. Fujii. Mechanisms of surface pressure distribution within a laminar separation bubble at different reynolds numbers. *Physics of Fluids*, 27(2), 2015. doi: https://doi.org/10.1063/1.4913500.

[25] M. Braune and A. Hebler. Sensitivity of single degree of freedom limit cycle flutter of a laminar airfoil and resulting uncertainties of the transonic dip. In A. Dillmann, G. Heller, E. Krämer, C. Wagner, S. Jakirlic, and C. Tropea, editors, *New Results in Numerical and Experimental Fluid Mechanics XII*, Notes on Numerical Fluid Mechanics and Multidisciplinary Design. Springer, 2019. Accepted for publication.

[26] H. Tijdeman and R. Seebass. Transonic flow past oscillating airfoils. *Annual Review of Fluid Mechanics*, 12:181-222, 1980. doi: https://doi.org/10.1146/annurev.fl.12.010180.001145.

[27] G. Schewe and H. Mai. Experiments on transonic limit-cycle-flutter of a flexible swept wing. *Journal of Fluids and Structures*, 84:153-170, 2019. doi: https://doi.org/10.1016/j.jfluidstructs.2018.07.005.